Nuclear Science and Techniques (2025) 36:35
https://doi.org/10.1007/s41365-024-01629-5

Investigations of inelastic cross sections of H_2O molecule by He^{2+} and C^{6+} projectiles with energy range around the Bragg peak

Guo-Zhuang Li[1,2,3] · Cheng-Ye Sun[2] · Rui Cheng[2,3] · Yan-Shi Zhang[2,3] · Liang-Wen Chen[2,3] · Sheng Zhang[2,4,5] · Xin-Xia Li[1] · Lei Yang[2,3,6]

Received: 29 March 2024 / Revised: 27 June 2024 / Accepted: 27 July 2024 / Published online: 14 January 2025

Abstract
Inelastic collisions are the dominant cause of energy loss in radiotherapy. In the energy range around the Bragg peak, single ionization (SI) and single-electron capture (SC) are the primary inelastic collisions that lead to energy loss. This study employs the classical trajectory Monte Carlo method to study the SI and SC processes of H_2O molecules using He^{2+} and C^{6+} projectiles in the energy range of 10 keV/u to 10 MeV/u. The total cross sections, single differential cross sections, impact parameter dependence of SI and SC, and fragmentation cross sections were investigated. Results illustrate that the cross section for SI is the highest when the projectile energy is close to the Bragg peak energy. When the projectile energy is below the Bragg peak energy, the ionized electrons in the forward direction dominate, and the removal of electrons can be associated with large impact parameters. As the projectile energy increases, the emission angle of the electrons gradually transitions from small angles (0° ∼ 30°) to large angles (60° ∼ 120°), and the removal of electrons is associated with small impact parameters. The energy distributions of the ionized electron are similar when the projectile energy is equal to, below or above the Bragg peak energy. The fragmentation cross sections after SI and SC in the energy range around the Bragg peak were also estimated.

Keywords Classical trajectory Monte Carlo · Heavy ion–water molecule collision · Inelastic cross sections

1 Introduction

Over the last two decades, heavy-ion radiation therapy has gained increasing interest [1–5], and many laboratories have been established to apply helium or carbon ion beams for therapy research [6–13]. Compared with photon therapy, heavy-ion therapy has several impressive advantages, including conformal dose distribution and high biological effectiveness in cell killing [14, 15], thus presenting heavy-ion

This work was supported in part by the National Natural Science Foundation of China (Nos. 12105327 and 11775108), the Hunan Provincial Innovation Foundation For Postgraduate (No. QL20220210) and the Advanced Energy Science and Technology Guangdong Laboratory.

✉ Liang-Wen Chen
chenlw@impcas.ac.cn

✉ Sheng Zhang
zhangsheng@njust.edu.cn

✉ Xin-Xia Li
li_xx@usc.edu.cn

[1] School of Nuclear Science and Technology, University of South China, Hengyang 421001, China

[2] Advanced Energy Science and Technology Guangdong Laboratory, Huizhou 516000, China

[3] Institute of Modern Physics, Chinese Academy of Sciences, Lanzhou 730000, China

[4] Interdisciplinary Center for Fundamental and Frontier Sciences, Nanjing University of Science and Technology, Jiangyin 214443, China

[5] Center for Basic Teaching and Experiment, Nanjing University of Science and Technology, Jiangyin 214443, China

[6] School of Nuclear Science and Technology, University of Chinese Academy of Sciences, Beijing 100049, China

therapy as a good option for treating radio-resistant and hypoxic tumors [16–19]. These advantages are generally attributed to the fact that the ions deposit most of their energy near the endpoint of their trajectories, thus leading to a strong localization of the dose, usually known as the Bragg peak. The energy deposited by heavy ions around the Bragg peak generates DNA damage, which is generally classified into two groups "direct and indirect damage" [20]. Direct damage is caused by low-energy electrons that are produced in the inelastic collisions of heavy ions with molecules. Further ionization is stimulated by these low-energy electrons, leading to single- or double-stranded breaks in the DNA. Indirect damage refers to the effects caused by intermediate species generated by the fragmentation processes associated with inelastic collisions [21]. These species can further react with water or diffuse into DNA, where they can trigger other reactions and damage the molecule. At least approximately 50% of the damage is due to the indirect effect [20]. Therefore, the investigation of energetic heavy ion–water molecule inelastic collisions plays a crucial role in heavy-ion radiotherapy [22] and is one of the most important topics in DNA damage research.

In the energy range around the Bragg peak, the energy loss of a heavy-ion beam primarily arises from single ionization (SI) and single-electron capture (SC) [23, 24]. Elastic collisions contribute to energy loss only at lower projectile energies ($E < 10$ keV/u) [25]. The corresponding datasets, including ionization, electron capture and fragmentation cross sections, along with the kinetic energy distributions of various primary and secondary species, are basic data for DNA radiation damage research. These cross sections have been investigated using both experimental and theoretical approaches.

Several studies have investigated the collisions of biological molecules that are subjected to energetic ions [26]. In the energy range around the Bragg peak, the total cross sections for ionization and/or electron capture of water molecules induced by different charged particles, encompassing electron [27], proton [28], helium ion [29], lithium ion [30] and carbon ion [31–33], have been studied experimentally. However, in terms of assessing differential cross sections in the energy range around the Bragg peak, the available experimental studies for heavy-ion projectiles are not extensive, with the majority of the existing results pertaining to light-ion projectiles such as H^+ or He^{2+} [34]. Differential cross-sectional measurements for heavy-ion projectiles are limited, with only a few experimental data available for C^{6+} [35] and O^{8+} [36] projectiles.

Many phenomenological models have been introduced to describe ion–water molecule inelastic collisions [37]. Uehara et al. [38] introduced a polynomial fit to describe the total cross sections of the SI process and single differential cross sections for protons and alpha particles at projectile energies below 300 keV/u. However, the constructed model tends to underestimate the cross sections at higher energies, and the discrepancies can be as large as 30% at a projectile energy of approximately 2 MeV/u [38]. Boudrioua et al. [39] and Champion et al. [40] conducted calculations using the first Born approximation (FBA) model for H^+ and He^{2+} projectiles in the projectile energy range of 0.1 MeV/u ~ 10 MeV/u, respectively. It should be noted that for heavier ions, such as carbon, the FBA model tends to overestimate the total cross sections at projectile energies below 1 MeV/u [41]. Various methods have been proposed to overcome the limitations of the FBA model, for example, quantum models such as the continuum distorted wave eikonal initial state model (CDW-EIS) [31, 42] and semiclassical methods such as the classical trajectory Monte Carlo (CTMC) method [41, 43]. Bhattacharjee et al. [31] applied the CDW-EIS method to calculate the single differential cross sections and total cross sections for C^{6+}, O^{8+} and Si^{13+} projectiles at 4 MeV/u. The results of the single differential cross sections were compared with experimental data and the results of the O^{8+} projectile exhibited better agreement than those of the other two projectiles. Liamsuwan et al. [41] employed the CTMC method with a one-center model potential to calculate the total cross sections and single differential cross sections for a C^{6+} projectile with energy in the range of 1 keV/u~1 MeV/u. The calculated single differential cross sections agreed well with the z^2 scaled proton results at projectile energies of 500 keV/u and 1 MeV/u, but a large deviation was observed for 100 keV/u. Bachi et al. [44] employed the CTMC method with a three-center model potential to calculate the total cross sections and single differential cross sections for 4 MeV/u C^{6+}, Si^{13+} and 3.75 MeV/u O^{8+} collisions on water molecules. Single differential cross sections show that the contribution of low electron energies is underestimated. Illescas et al. [45] first estimated the cross sections for molecular fragmentation after electron removal for H^+ projectiles. The fragmentation cross sections of H_2O^+ and OH^+ were in satisfactory agreement with the experimental data, whereas the results of OH^+ and H^+ were underestimated at low projectile energies. To our knowledge, for heavier ions like He^{2+} and C^{6+} projectiles, the water molecular fragmentation cross sections have not been investigated yet.

To the best of our knowledge, the available theoretical studies on heavy ions discussed in the literature survey have primarily focused on the total cross sections with a narrow energy range and the differential cross sections with a single energy. During heavy-ion penetration in water, significant energy loss is commonly observed in the energy range around the Bragg peak [25, 46, 47]. Therefore, one of the objectives of this study is to provide data for simulations of the damage caused by heavy ions in the energy range around the Bragg peak. In this study, we focus on the more frequently employed ion beams in heavy-ion radiotherapy,

namely helium and carbon ions. On the other hand, the fundamental data at the Bragg peak energy and energies below as well as above the Bragg peak energy are investigated. These results include the total cross sections, single differential cross sections, impact parameter dependence of the SI and SC, and fragmentation cross sections.

The remainder of this paper is organized as follows. In Sect. 2, we introduce the method applied to the calculations. In Sect. 3, we present the results of the SI and SC total cross sections, single differential cross sections, impact parameter dependence and fragmentation cross sections for He^{2+} and C^{6+} projectiles. Finally, the conclusions are provided.

2 Numerical method

In this work, the cross sections are calculated using the CTMC method. This method is based on simultaneous trajectory simulations of the collision partners, which include the screened target, projectile charged particle and active electron. Owing to the convenient description of the interactions between collision partners provided by classical Newtonian mechanics, this approach is particularly suitable for studying charged particle collisions with energies ranging from a few tens of keV/u to tens of MeV/u.

For multi-electron collision systems, two methods are employed for calculating the cross sections: the independent electron model (IEM) and the independent event model (IEVM). In the IEM, the second electron is still considered to be bound in the H_2O molecule after the first electron is removed. For the IEVM, it is assumed that electron removal occurs sequentially, which means that the second electron is attached or removed from H_2O^+ [45]. Therefore, the IEVM is more effective than the IEM in treating multi-electron collision systems; this study employs the IEVM method for calculating cross sections, including impact parameter dependence. The ion–water molecular collision system is treated as a three-body collision system. The Hamiltonian of the three-body ion–water collision system can be written as

$$\begin{aligned}\boldsymbol{H} = & \frac{p_A^2}{2M_A} + \frac{p_B^2}{2M_B} + \frac{p_C^2}{2} + V_{AB}(\boldsymbol{R}_{AB}) \\ & + V_{AC}(\boldsymbol{R}_{AC}) + V_{BC}(\boldsymbol{R}_{BC}),\end{aligned} \tag{1}$$

where M_i and p_i denote the mass and momenta for charged particles, respectively. A, B and C are the indices of the projectile, H_2O^+ ion and active electron, respectively. R is the distance between the different particles. The first three terms present the kinetic energies of the three particles, and the next three terms are the interaction potentials of the collision system. Note that atomic units are adopted throughout this paper unless otherwise stated.

In the CTMC method, both one- and three-center model potentials have been proposed to describe water molecular targets [41, 44]. The former treats the water molecule target as an atom with a nuclear charge of 10, whereas the latter incorporates two hydrogen atoms and one oxygen atom to describe the water molecular target. The three-center model potential provides a detailed representation of the anisotropy of the molecular target; however, it entails a more complex interaction potential (see Ref. [45]). This study adapts the one-center model potential $V_{ij}(r)$ proposed in Ref. [48]. The interaction potentials in Eq.(1) between the different charged particles are given by

$$V_{ij}(r) = \begin{cases} \frac{Z_{\mathrm{eff},i}(r)Z_{\mathrm{eff},j}(r)}{r}, i = A, j = B \\ \frac{Z_{\mathrm{eff},i}(r)}{r}, i = A \text{ or } B, j = C \end{cases} \tag{2}$$

$$Z_{\mathrm{eff},i}(r) = Z_i - N_i[1 - \Omega_i(r)], \tag{3}$$

$$\Omega_i(r) = \frac{1}{\left(\frac{\eta_i}{\zeta_i}\right)\left(e^{\zeta_i r} - 1\right) + 1}, \tag{4}$$

and

$$\eta_i = \eta_{0,i} + \eta_{1,i}(Z_i - N_i - 1), \tag{5}$$

$$\zeta_i = \zeta_{0,i} + \zeta_{1,i}(Z_i - N_i - 1), \tag{6}$$

where Z_i is the bare nuclear charge of the projectile ion or H_2O^+ ion; N_i represents the count of spectator electrons attached to the core; and $\Omega_i(r)$ denotes the screening function described by the screening parameters (η_i, ζ_i, $\zeta_{0,i}$, $\eta_{0,i}$, $\eta_{1,i}$ and $\zeta_{1,i}$). The index i represents a specific particle. (For simplicity, the index is omitted from the subsequent content.) Equation (3) illustrates H_2O^+, which appears as an exposed nucleus when the collision partner is in proximity and becomes entirely shielded by the spectator electrons when the separation distance becomes infinitely large. For the target (H_2O^+) and projectiles (H^+, He^{2+} and C^{6+}) under investigation, the number of spectator electrons N and the screening parameters η_0 and ζ_0 are taken from Ref. [48], as listed in Table 1. The screening parameters η_1 and ζ_1 can be

Table 1 Number of spectator electrons N and the screening parameters (ζ_0 and η_0) used in the effective charge formula (Eqs. 3–6) for different targets and projectiles

Ion species	N	ζ_0	η_0
H^+, He^{2+} and C^{6+}	0	1	0
H_2O	9	1.792	2.710

neglected because Z=10 and N=9. The water molecule target was represented as a spherically symmetric atom possessing binding energies identical to those of a water molecule (Table 2) and nuclear charge of Z=10. The binding energy is required for calculating the initial position and momentum of the active electron. A detailed description can be found in Ref. [49]. The initial distribution of each molecular orbital is determined using the method described in Ref [43], and the distributions are consistent with those in ref. [43].

The fragmentation cross sections that arise from the SI and SC processes were also investigated. When a water molecule undergoes fragmentation due to ionizing radiation, whether through collisions with photons, electrons or heavy ions, it can break into two or three components after single-electron removal (SI and SC processes for ion–H_2O collisions). The fragmentation pattern is independent of the projectile type and is mainly determined by the energy transferred during the collision as well as the specific molecular orbital where a primary vacancy is generated [50]. For high-energy electron projectiles, branching ratios for fragmentation have been proposed by estimating the experimental data [51]. Therefore, the fragmentation cross sections can be computed by multiplying the corresponding branching ratios.

$$\begin{aligned}
\sigma_{H_2O^+}^{SC,SI} &= 1.00\sigma^{SC,SI}(1b_1) + 1.00\sigma^{SC,SI}(3a_1) \\
&\quad + 0.08\sigma^{SC,SI}(1b_2), \\
\sigma_{OH}^{SC,SI} &= 0.70\sigma^{SC,SI}(1b_2), \\
\sigma_{H^+}^{SC,SI} &= 0.22\sigma^{SC,SI}(1b_2)+0.74\sigma^{SC,SI}(2a_1), \\
\sigma_{O^+}^{SC,SI} &= 0.26\sigma^{SC,SI}(2a_1).
\end{aligned} \tag{7}$$

The computation of fragmentation cross sections has primarily focused on the H^+ projectile in practical applications. For projectiles with different charges, the fragmentation cross sections can be derived using Eq. (7) [45, 50].

Table 2 Electron binding energies of water; N_L denotes the effective number of active electrons for each orbital of the target

Orbital	Binding energy (eV)	N_L
$1b_1$	12.62	2
$3a_1$	14.75	2
$1b_2$	18.51	2
$2a_1$	32.40	2
$1a_1$	539.7	2

3 Results and discussion

This study conducts a detailed investigation of the ion–water molecule collision involving He^{2+} and C^{6+} projectiles. First, an extensive comparison between the results obtained using our CTMC code, experimental data and representative theoretical results is provided. Subsequently, the total cross sections and single differential cross sections, as well as the impact parameter dependence of SI and SC for the five molecular orbitals, are discussed. Fragmentation cross sections of the water molecules were also obtained.

The relative uncertainty of the cross section is given by [52]

$$\Delta\sigma_i/\sigma_i = [(N - N_i)/NN_i]^{1/2}, \tag{8}$$

where σ_i is the cross section and i is the index for different reactions. N and N_i are the initial number of trajectories and output number of trajectories for different reactions, respectively. These cross-sectional calculations were performed with at least 10,000 trajectories, and the relative uncertainty was less than 15%. A slight difference was observed when different input parameters, such as the time step and initial distance between the projectile ion and target, were selected. The effects of these input parameters are discussed in our previous study [52].

3.1 Comparison of experimental and theoretical results

The SI and SC total cross sections for the fully stripped ion (He^{2+} and C^{6+})–water molecule collisions in the energy range around the Bragg peak were calculated to compare our results with the available experimental and theoretical results. Additionally, single differential cross sections for the C^{6+} projectile at 4 MeV/u, as well as fragmentation cross sections for the H^+ projectiles, are presented.

Figure 1 presents a comparative analysis of the total cross sections of SI and SC. This includes the results obtained using our CTMC code, experimental data [31, 40, 53] and other theoretical results. In Fig. 1a, the total cross sections for the SI calculated using our CTMC code for He^{2+}+H_2O agree well with the experimental data. The FBA results for the C^{6+}+H_2O collision include those obtained from ref. [53]. Notably, the CTMC results exhibit better agreement with the experimental data than the FBA results. Moreover, our results for C^{6+}+H_2O agree well with calculation provided by Liamsuwan [41], which utilized the CTMC method with the one-center model potential and the IEVM. Figure 1b presents a comparison of the total cross sections of the SC. Good agreement was found between the results of our CTMC code and the experimental data. As no experimental

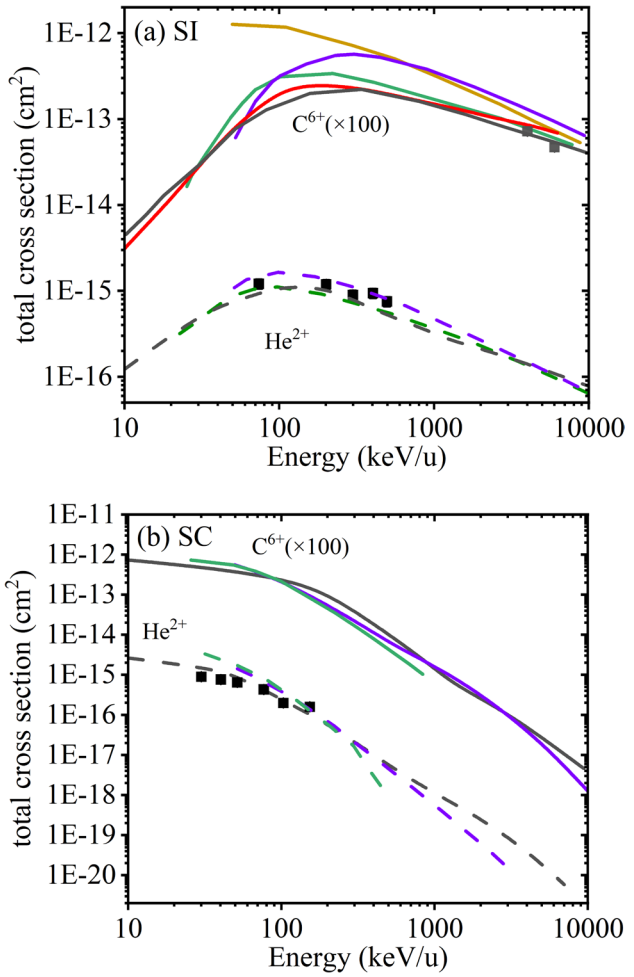

Fig. 1 (Color online) **a** SI and **b** SC total cross sections for $He^{2+}+H_2O$ (dashed line) and $C^{6+}+H_2O$ (solid line) collisions. The results obtained using our CTMC code (black line), CTMC results by Liamsuwan [41] (red line), CTMC results by Illescas [45] (green line), FBA results by Dal Cappello [53] (yellow line), CDW-EIS results by Quinto [42] (purple line) and experimental data taken from different sources [31, 40, 53] (black solid squares)

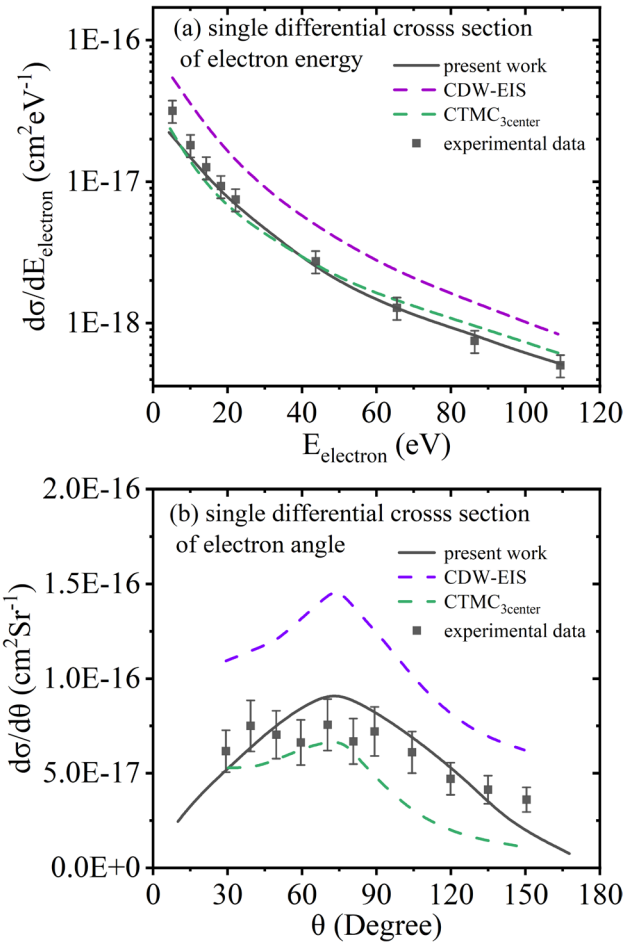

Fig. 2 (Color online) Single differential cross sections of electron **a** energy and **b** angle for $C^{6+}+H_2O$ collision at 4 MeV/u. The results of this work were obtained using our CTMC code (black solid line). Results by the CDW-EIS method (purple dashed line) [31]. Results by the $CTMC_{3\text{-center}}$ method (green dashed line) [44]; Experimental data (black solid squares) [31]

data exist for SC cross sections for carbon ions, we compared our CTMC results with CDW-EIS [24] and found good agreement.

In Fig. 2, we present a comparison of single differential cross sections obtained using our CTMC code with experimental data [31] as well as other theoretical results (CDW-EIS results from Ref.[31] and $CTMC_{3\text{-center}}$ results from Ref. [44]). Figure 2a shows the single differential cross sections of the electron energy for $C^{6+}+H_2O$ collisions at 4 MeV/u. The CTMC results agree well with those of $CTMC_{3\text{-center}}$. The experimental data were in better agreement with our CTMC results than with those obtained using the CDW-EIS method. Figure 2b illustrates the single differential cross sections of the electron angle. $CTMC_{3\text{-center}}$ and CDW-EIS results exhibited a similar profile for the single differential cross sections, featuring a peak around a 75° angle. Although our CTMC results also display a maximum at approximately the same emission angle, the overall spectral behavior exhibits a slight difference.

Figure 3 compares the fragmentation cross sections of H_2O^+, OH^+, H^+ and O^+ fragments after the SI and SC processes for H^++H_2O. The results for the fragmentation cross sections obtained using our CTMC code and the experimental data from Ref. [29] and the theoretical results of Ref. [45] are illustrated. Our CTMC results illustrated in the upper panel that examine the fragmentation cross sections after SI agree well with those in Ref. [45]. However, our results regarding H^+ and O^+ show deviations within 50% compared with the experimental data from Ref. [29] for projectile energies below 500 keV/u. The lower panel presents our CTMC results for fragmentation cross sections after SC and reveals

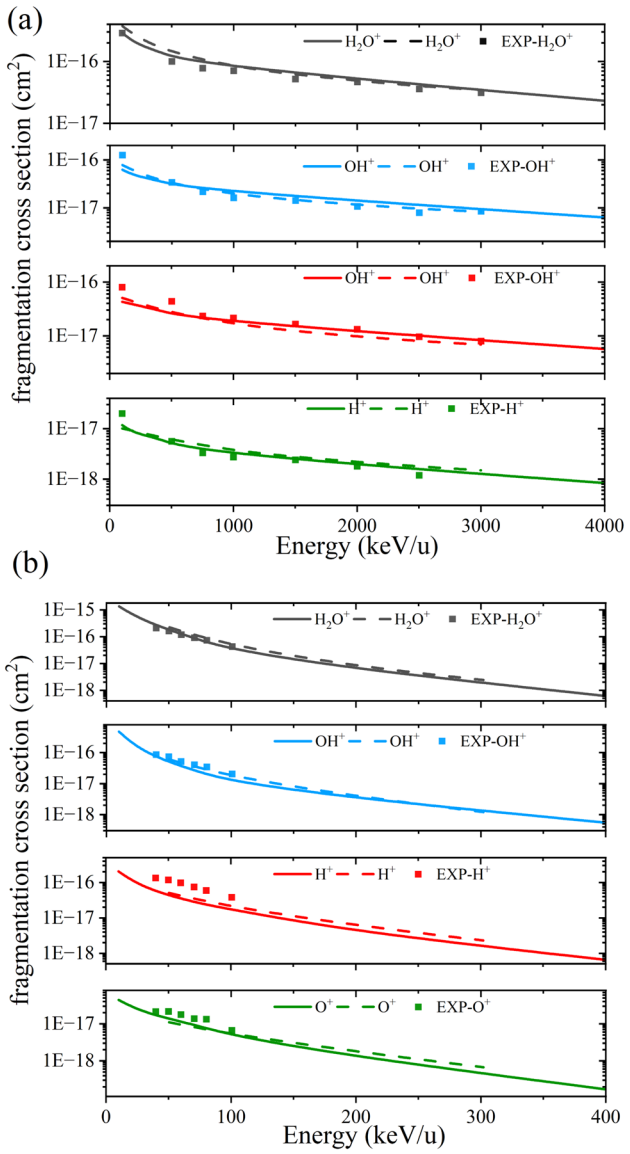

Fig. 3 (Color online) Fragmentation cross sections of H_2O^+, OH^+, H^+ and O^+ fragments following the (upper panel) SI and (lower panel) SC processes in H^++H_2O collisions (solid line), theoretical results of Ref. [45] (dashed line) and experimental data of Ref. [29] (solid squares)

underestimations of the results of H^+ and O^+ by approximately 30% of the experimental data at low projectile energies (E<100 keV/u). The observed discrepancy in the fragmentation cross sections after the SI and SC processes can be attributed to the underestimated partial cross section of the $2a_1$ molecular orbital [45]. Nevertheless, for the H_2O^+ and OH^+ fragments, our results exhibit satisfactory agreement with the experimental data.

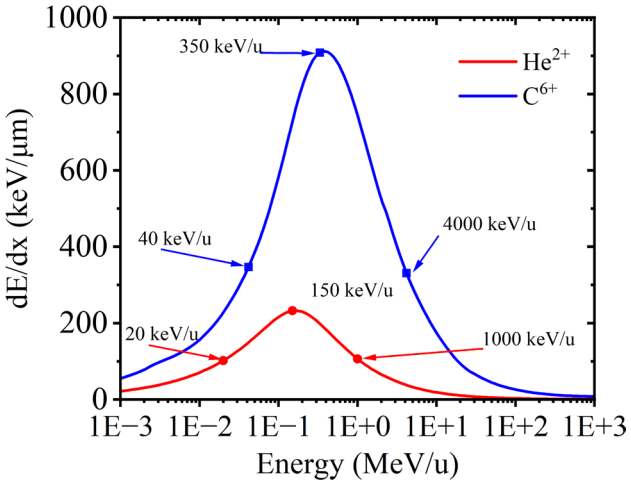

Fig. 4 (Color online) The specific energy loss dE/dx of He^{2+} and C^{6+} ions in water was calculated using the SRIM (Stopping and Range of Ions in Matter) software [54]. For convenience, the specific energies selected are plotted

3.2 Single differential cross sections for He^{2+} and C^{6+} projectiles

In this subsection, the single differential cross sections of the electron energy and angle for the specific projectile energy range around the Bragg peak are investigated. Figure 4 shows the energy loss of He^{2+} and C^{6+} ions in water, calculated using the SRIM software [54]. The atomic number of the projectile ions (helium and carbon) and energy range (1 keV/u~1000 MeV/u) are required to calculate the energy loss curves. Moreover, the element species and the corresponding atomic percent (0.67 for hydrogen and 0.33 for oxygen) for H_2O should be provided. The region of high energy loss of helium and carbon ions in water is defined as the Bragg peak region. The projectile energy range of the Bragg peak region is defined as the energy range around the Bragg peak according to the SRIM calculation results. The projectile energy with the maximum energy loss is defined as the Bragg peak energy. Apart from the projectile energy with the maximum energy loss, we also chose two projectiles with similar energy losses: One was lower than the Bragg peak energy, and the other was greater. The selected representative projectile energies and the corresponding total cross sections of the SI for C^{6+} and He^{2+} are listed in Table 3. In combination with the total cross sections of the SI in Fig. 1a, we determined that the total cross section is the highest when the projectile energy is close to the Bragg peak energy. A "one peak structure" is present for the total cross sections of SI in the energy range around the Bragg peak.

The single differential cross sections of the electron energy for He^{2+}+H_2O and C^{6+}+H_2O collisions at specific

Table 3 Selected projectile energies and corresponding SI cross section for C^{6+} and He^{2+} around the Bragg peak

Projectile	Projectile energies (keV/u)	d*E*/d*x* (keV/μm)	SI cross section (cm^2)
He^{2+}	20	101.9	4.0×10^{-16}
	150	232.2	1.0×10^{-15}
	1000	106.4	3.0×10^{-16}
C^{6+}	40	347.2	5.5×10^{-16}
	350	908.5	1.4×10^{-15}
	4000	333.1	6.9×10^{-16}

projectile energies are shown in Fig. 5a and b, respectively. The energy distributions for the different projectile energies exhibited a similar shape. The single differential cross sections decreased as the electron energy increased. The percentage of low-energy electrons (<20 eV) was above 50% in both He^{2+} and C^{6+} projectiles. Consequently, it can be inferred that the energy distributions of the electrons are similar when the projectile energy is equal to, below or above the Bragg peak energy.

Figure 6a and b presents the single differential cross sections of the electron angle for He^{2+}+H_2O and C^{6+}+H_2O collisions, respectively. Low-energy projectiles tend to ionize electrons in a nearly forward direction (0° ~ 30°). At higher projectile energies, ionized electrons tend to be emitted at larger angles (60° ~ 120°). In the classical description of ionization, when the projectile velocity is much lower than the ionization cross-sectional maximum (as in the case shown in Fig. 1, 350 keV/u for C^{6+} and 150 keV/u for He^{2+}), the primary mechanism is saddle-point ionization. The longitudinal momentum of the ionized electrons was greater than zero, and there was an asymmetric shell of ionizing electrons in the direction of the

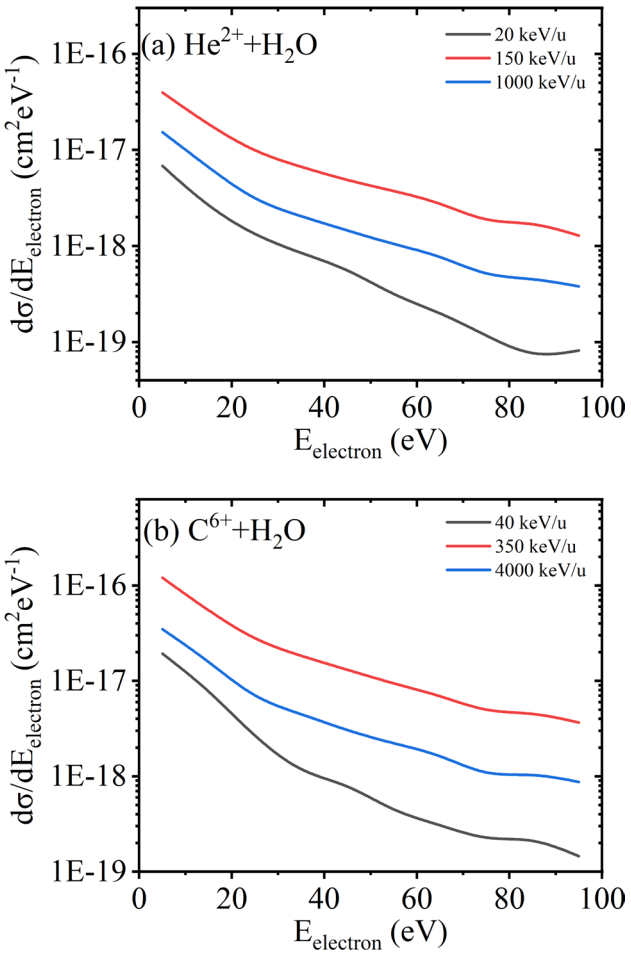

Fig. 5 (Color online) Single differential cross sections of electron energy for **a** He^{2+}+H_2O and **b** C^{6+}+H_2O collisions at specific projectile energy range around the Bragg peak (20 keV/u, 150 keV/u and 1000 keV/u for He^{2+}; 40 keV/u, 350 keV/u and 4000 keV/u for C^{6+})

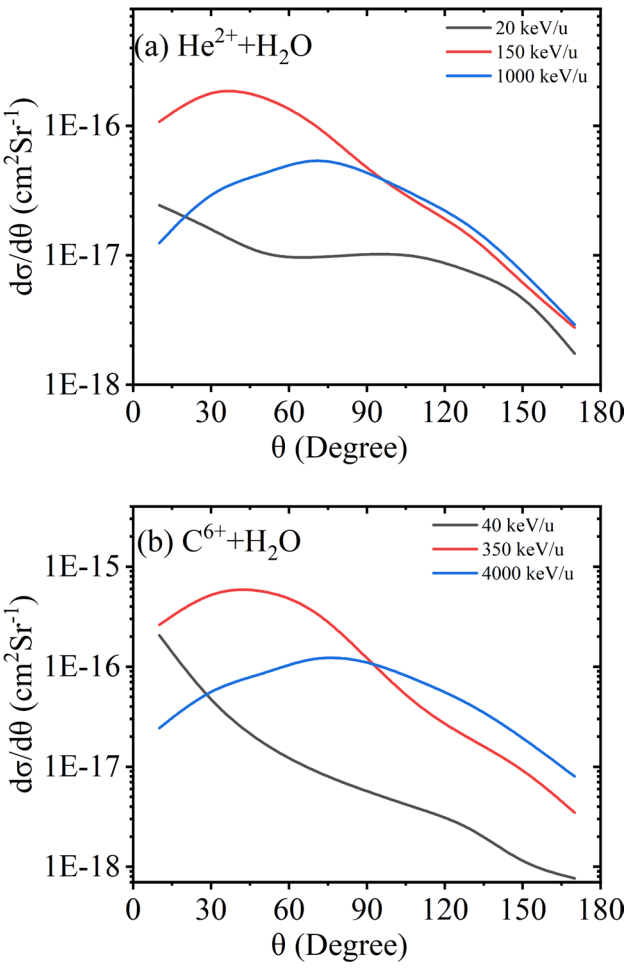

Fig. 6 (Color online) Single differential cross sections of electron angle for **a** He^{2+}+H_2O and **b** C^{6+}+H_2O collision at specific projectile energy range around the Bragg peak (20 keV/u, 150 keV/u and 1000 keV/u for He^{2+}; 40 keV/u, 350 keV/u and 4000 keV/u for C^{6+})

projectile. As the projectile energy increases, saddle-point ionization is replaced by a direct ionization mechanism in which most electrons depart with a longitudinal momentum close to zero [55]. This results in larger emission angles at higher projectile energies. This effect has also been observed in ion–atom collisions [56]. Projectile energies higher than the Bragg peak energy were smaller at lower angles of 15° ∼ 30°. This can be described by the forward–backward asymmetry parameter (FBPA) [28], which is essential for understanding the electron angular distribution. The FBPA was calculated as follows:

$$\alpha(\theta) = \frac{\sigma(\theta) - \sigma(\pi - \theta)}{\sigma(\theta) + \sigma(\pi - \theta)}, \tag{9}$$

where $\sigma(\theta)$ and $\sigma(\pi - \theta)$ denote the absolute single differential cross section at the lowest forward angle (θ) and its exact opposite backward angle ($\pi - \theta$), respectively. We calculated the FBPA at θ=15°, as listed in Table 4. The results show that the FBPA at projectile energies above the Bragg peak energy is lower than that at projectile energies below or equal to the Bragg peak energy. This trend indicates that the gap between the proportions of forward (0° ∼ 15°) and backward (165° ∼ 180°) ionized electrons is smaller for projectile energies above the Bragg peak energy. Based on the results for the single differential cross section of the electron angle, it was observed that when the projectile energy is lower, equal to or higher than the Bragg peak energy, the emission angle of the electrons gradually transitions from small angles (0° ∼ 30°) to large angles (60° ∼ 120°).

3.3 Impact parameter dependence for He^{2+}+H_2O and C^{6+}+H_2O collisions

In this subsection, the percentage of the ionized electrons from the five molecular orbitals for different impact parameter ranges are discussed. The impact parameter dependence $P_L(b)$ is the normalized single differential cross section of the impact parameter, which is expressed in terms of

Table 4 FBPA at different projectiles for He^{2+} and C^{6+} using θ=15°

Projectile	Projectile energies (keV/u)	FBPA
He^{2+}	20	0.87
	150	0.94
	1000	0.69
C^{6+}	40	0.92
	350	0.94
	4000	0.52

$$P_L(b) = \frac{d\sigma_L(b)}{db} \Big/ \left(\frac{d\sigma(b)}{db}\right)_{max}, \tag{10}$$

where $\frac{d\sigma_L(b)}{db}$ is the single differential cross section of impact parameter for a specific molecule orbital, and index L denotes different molecular orbitals. $\left(\frac{d\sigma(b)}{db}\right)_{max}$ is the maximum value of the single differential cross section of the impact parameter dependence for the five molecular orbitals. $P_L(b)$ for the five molecular orbitals (yellow curve) are also presented, which reflects the contribution of each orbital to the SI or SC processes for different impact parameter ranges. This directly results in different fragmentation cross sections, as indicated in the next subsection. The contribution of each orbital as a function of the impact parameter is of particular significance [57]. This information constitutes input data for the Monte Carlo simulation code [58].

Figure 7 shows the results for projectile energies of 20, 150 and 1000 keV/u. The impact parameter dependence of the SI does not exhibit a significant difference for different projectile energies, which implies that the contribution of each orbital is similar at different projectile energies. The impact parameter dependence for each orbital and its total generally increased and then decreased as the impact parameter increased. This behavior is attributed to the prevalence of multi-electron processes over single-electron processes in a small impact parameter range [44]. However, the excitation processes become dominant for large impact parameters. Consequently, the SI process appears to dominate in the medium impact parameter regions, for example, 1 ∼ 3 a.u. is the region where SI dominates for 150 keV/u He^{2+}, as shown in Fig. 7b, where the atomic unit of length (a.u.) is the classical Bohr radius a_0 of the ground state electron. With respect to the contributions of the molecular orbitals, there is a negative correlation with the corresponding binding energies. A higher binding energy of the molecular orbitals is attributed with a smaller peak value of the impact parameters and larger impact parameter corresponding to the peak position. For example, in the case of 150 keV/u shown in Fig. 7b, the ionized electrons in the large impact region are mainly lower binding energy electrons (E_{1b_1} ∼12.62 eV, E_{3a_1} ∼14.75 eV and E_{1b_2} ∼18.51 eV). This result conforms to our intuition and experience with ion–atom collisions. It is well known that an electron from an orbital with a lower binding energy is more easily pulled out by a projectile. Moreover, for variations in the impact parameter dependence around the Bragg peak, electrons tend to be ionized in the large impact parameter when the projectile energy is below the Bragg peak energy. When the projectile energy exceeds the Bragg peak energy, the electrons tend to be ionized with a small impact parameter.

For the SC of the He^{2+} projectile shown in Fig. 8, one can see that the contributions of $1b_1$, $2a_1$ and $1a_1$

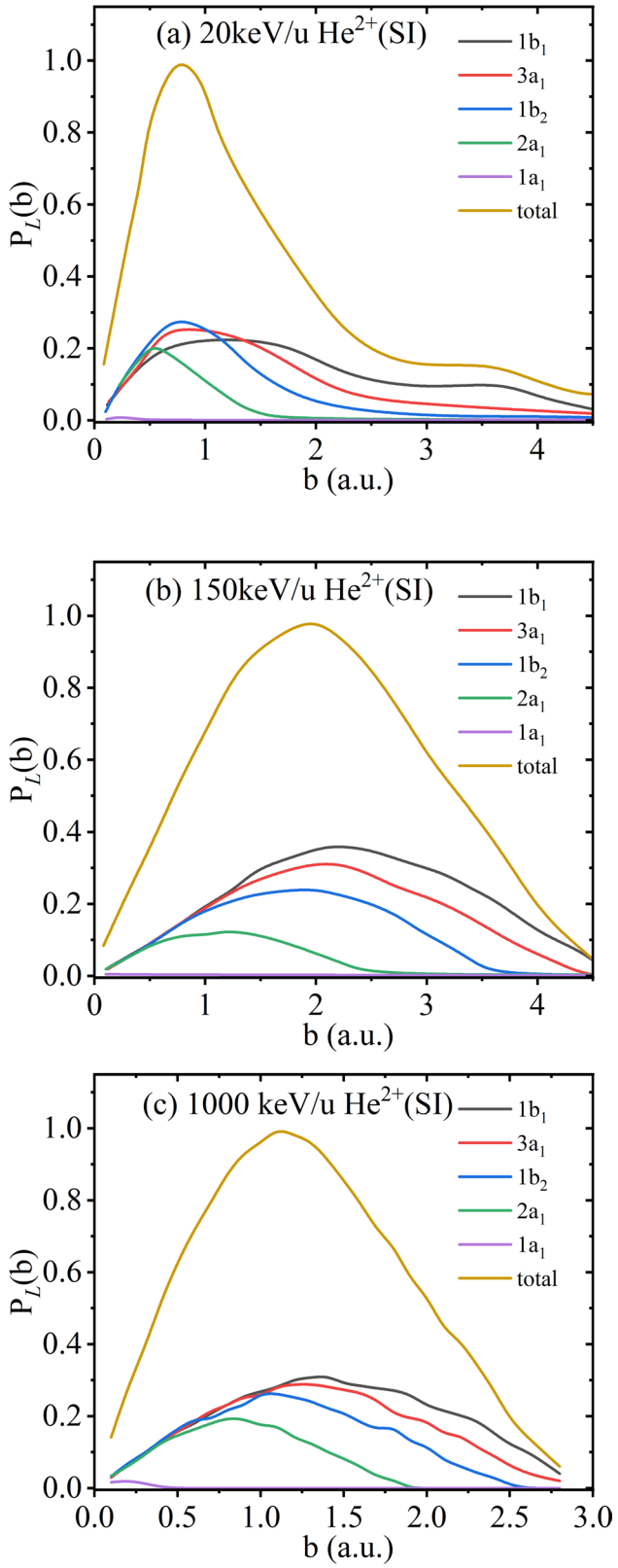

Fig. 7 (Color online) Impact parameter dependence of SI for $1a_1$ (purple), $1b_1$ (black), $1b_2$ (blue), $2a_1$ (green) and $3a_1$ (red) molecular orbitals as well as the sum of five molecular orbitals (yellow) for He^{2+} projectile at **a** 20 keV/u, **b** 150 keV/u and **c** 1000 keV/u

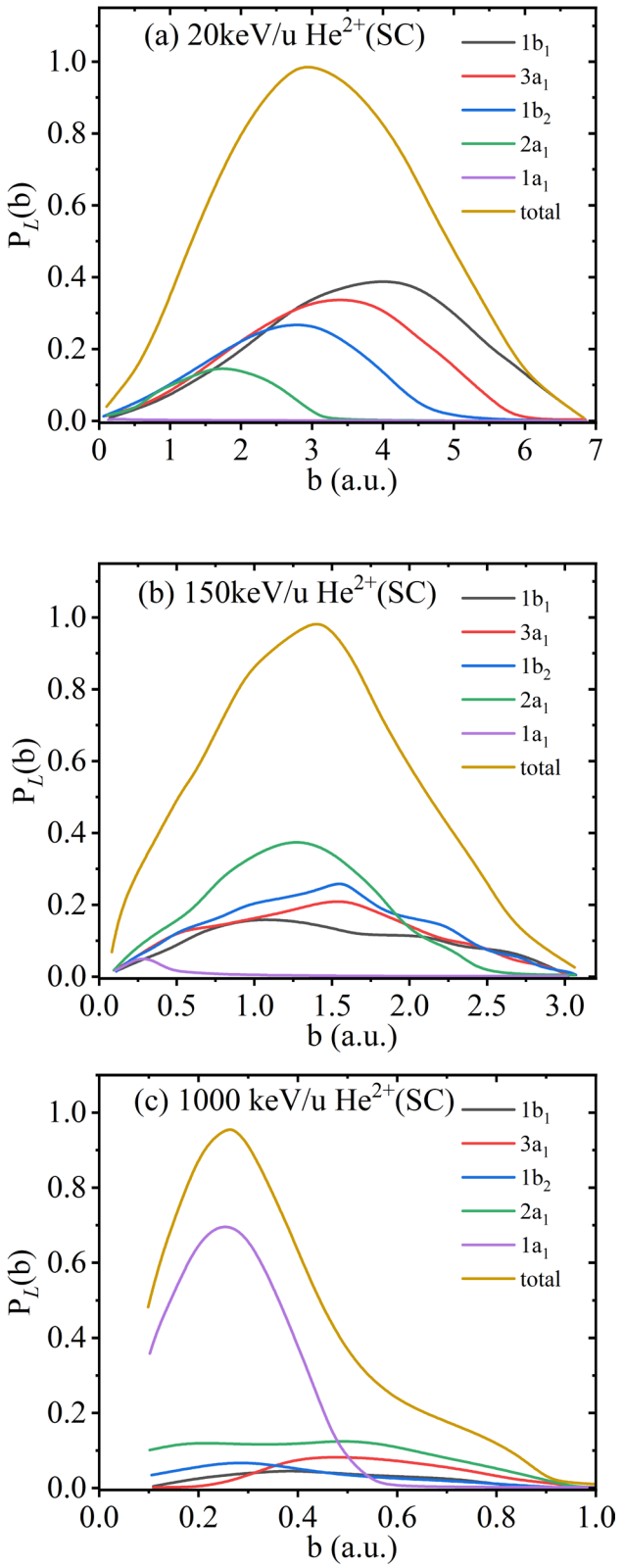

Fig. 8 (Color online) Impact parameter dependence of SC for $1a_1$ (purple), $1b_1$ (black), $1b_2$ (blue), $2a_1$ (green) and $3a_1$ (red) molecular orbitals as well as the sum of five molecular orbitals (yellow) for the He^{2+} projectile at **a** 20 keV/u, **b** 150 keV/u and **c** 1000 keV/u

orbitals dominate at 20, 150 and 1000 keV/u, respectively. This behavior is observed because a bound electron with a velocity closer to that of the projectile is more likely to be captured by the projectile [42]. The velocities of the bound electron and the He^{2+} projectile with an energy of 1000 keV/u can be easily obtained, that is, $v_{1b_1} \sim 0.0070c$, $v_{3a_1} \sim 0.0076c$, $v_{1b_2} \sim 0.0085c$, $v_{2a_1} \sim 0.0113c$, $v_{1a_1} \sim 0.0459c$, $v_{He} \sim 0.0921c$, where c is the speed of light. Among the bound electrons, the velocity of the $1a_1$ electron is the closest to that of the He^{2+} projectile with an energy of 1000 keV/u. Consequently, the $1a_1$ electrons dominate the SC process. By comparing the impact parameter dependence of SC around the Bragg peak, it can be concluded that when the electron velocity is close to that of the projectile, the corresponding orbital dominates the SC process.

The impact parameter dependence of SI for the C^{6+} projectile at 40, 350 and 4000 keV/u is shown in Fig. 9. A behavior similar to that of the He^{2+} projectile was observed. A "one peak structure" for the impact parameter dependence of the five orbitals is present. Furthermore, for the result at 40 keV/u shown in panel (a), there is a "bimodal structure" for impact parameter dependence of the sum (yellow curve) that has not been observed in other cases. This structure is observed because electrons dominate different impact parameter regions for different orbitals. Then, the superposition of the individual orbitals leads to a "bimodal structure". For example, for the results of 40 keV/u, the ionized electrons from the $1a_1$ and $2a_1$ orbitals dominate in the small impact parameter range ($0 < b < 3$), and those from the $1b_1$, $3a_1$ and $1b_2$ orbitals dominate in large impact parameter range ($3 < b < 10$). Therefore, the "bimodal structure" for impact parameter dependence of the sum at 40 keV/u is generated.

The SC parameter dependence of the C^{6+} projectile at 40keV/u, 350 keV/u and 4000 keV/u is shown in Fig. 10. The SC process showed a trend similar to that of the results for the He^{2+} projectile, where the dominance of the impact parameter dependence for a specific orbital depends on whether the electron velocity is close to the projectile velocity. In particular, for the results at 4000 keV/u, nearly all the capture processes are contributed by the $1a_1$ orbital. It can be anticipated that as the projectile energy increases, the capture process will be entirely contributed by the $1a_1$ orbital. However, it should be noted that at higher projectile energies, the SC cross section is significantly lower than the SI cross section (several orders of magnitude). Consequently, the contribution of specific orbitals to the SC process is no longer a critical factor.

The following conclusions can be drawn based on the current results regarding the impact parameter dependence: (i) For the impact parameter dependence of SI and SC, when the projectile energy is below the Bragg peak energy, the removal

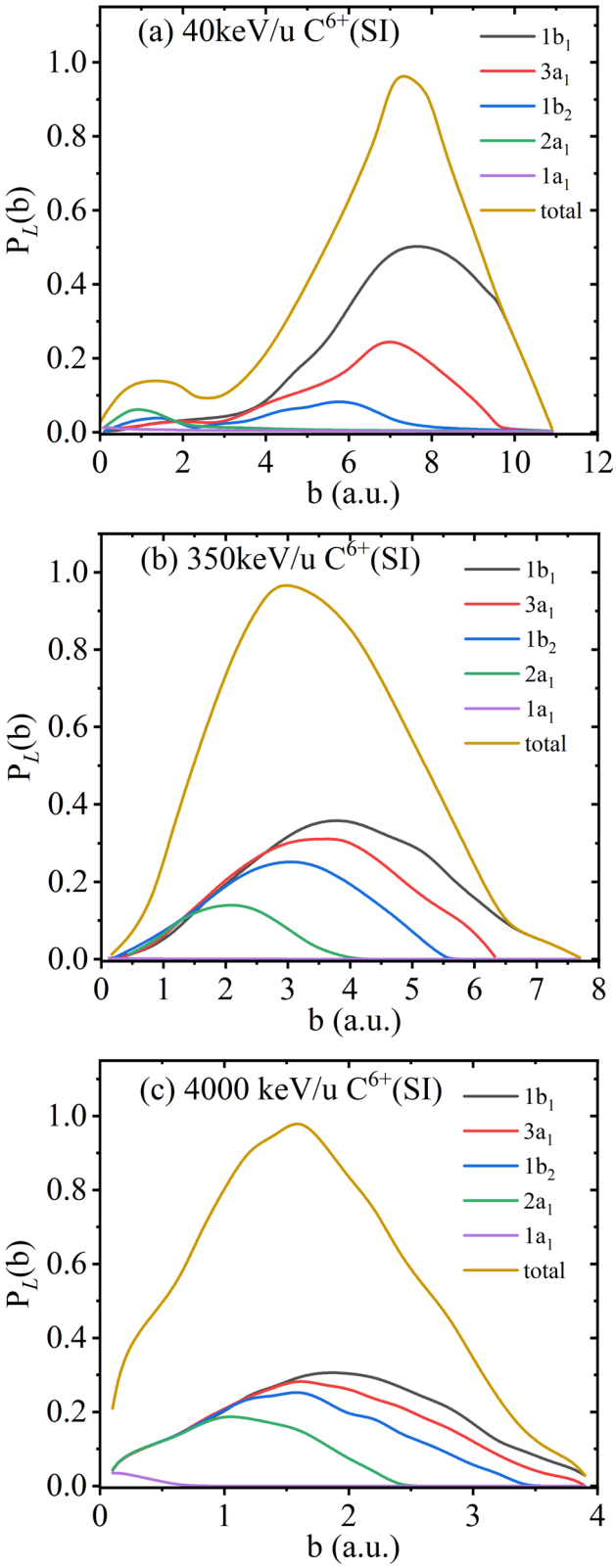

Fig. 9 (Color online) Impact parameter dependence of SI for $1a_1$ (purple), $1b_1$ (black), $1b_2$ (blue), $2a_1$ (green) and $3a_1$ (red) molecular orbitals as well as the sum of five molecular orbitals (yellow) for C^{6+} projectile at **a** 40 keV/u, **b** 350 keV/u and **c** 4000 keV/u

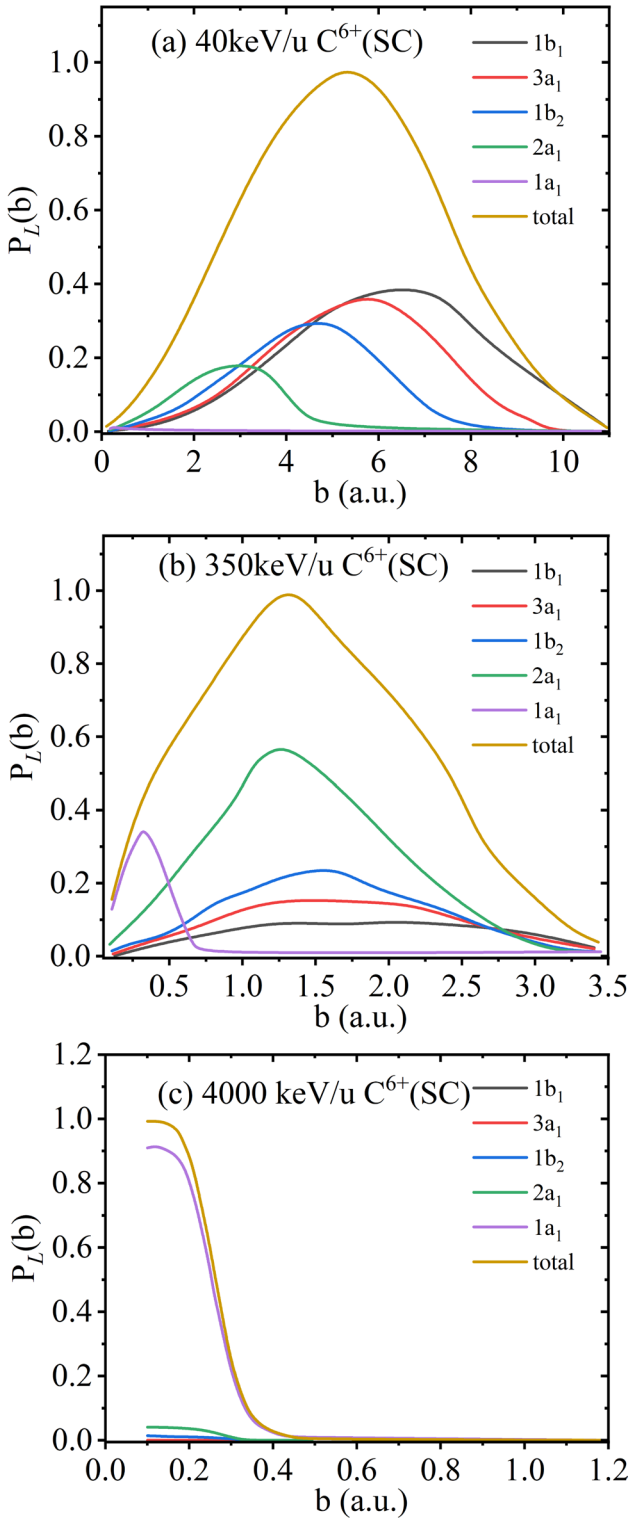

Fig. 10 (Color online) Impact parameter dependence of SC for $1a_1$ (purple), $1b_1$ (black), $1b_2$ (blue), $2a_1$ (green) and $3a_1$ (red) molecular orbitals as well as the sum of five molecular orbitals (yellow) for the C^{6+} projectile at **a** 40 keV/u, **b** 350 keV/u and **c** 4000 keV/u

of electrons (SI and SC processes) can be associated with larger impact parameters. As the projectile energy increases, the removal of electrons can be associated with small impact parameters. (ii) Regarding the impact parameter dependence of the SC, the dominance of a particular orbital at different projectile energies depends on whether the electron velocity is close to the projectile velocity. (iii) At different energies, each molecular orbit exhibits a "one peak structure" of the impact parameter dependence. In contrast, the impact parameter dependence of the sum must consider the superposition of the individual orbitals, perhaps with a "bimodal structure".

3.4 Fragmentation cross sections for He^{2+}+H_2O and C^{6+}+H_2O collisions

The fragmentation cross sections significantly influence the radiation damage caused by heavy-ion beams to biological systems, which is deemed the primary factor contributing to indirect DNA damage [7]. The fragmentation cross sections for He^{2+}+H_2O and C^{6+}+H_2O collisions are investigated in the following paragraphs.

The fragmentation cross sections after SI and SC for He^{2+} +H_2O and C^{6+}+H_2O collisions are shown in Fig. 11. In the fragmentation cross sections after SI, as shown in Fig. 11a, the cross section of each fragment increases and then decreases as the projectile energy increases. These curves are nearly parallel because the contributions of the $1b_1$, $2a_1$, $3a_1$ and $1b_2$ orbitals to the ionization remain nearly constant as the projectile energy increases [42]. Regarding the fragmentation cross sections after SC, as shown in Fig. 11b, the cross sections of each fragment decrease as the projectile energy increases. As expected, the lines representing the fragments H^+ and O^+, as well as H_2O^+ and OH^+, exhibit parallel behavior. Although the fragmentation cross sections after SC at energies above 700 keV/u are not presented, it can be predicted that the cross section of H^+ will be higher than that of H_2O^+ and the cross section of O^+ will be higher than that of OH^+ with projectile energy increase. For example, for the C^{6+} projectile, the H^+ fragmentation cross section is lower than that of H_2O^+ at 40 keV/u, whereas at 4000 keV/u, it can be predicted that the H^+ fragmentation cross section will be higher than that of H_2O^+. This trend can be attributed to the increasing contribution of the $2a_1$ orbital, which primarily influences the fragmentation cross sections of the H^+ and O^+ fragments after SC. As the projectile energy increases, the energy dependence of the $2a_1$ orbital changes the slope of the H^+ and O^+ lines but does not affect the other two lines.

Three conclusions can be drawn from these results: (i) In the energy range below the Bragg peak energy, the fragmentation cross section after SI increases and then decreases as the projectile energy increases, and the fragmentation cross section after SC decreases as the projectile energy increases. (ii) In the energy range above the Bragg peak energy, the

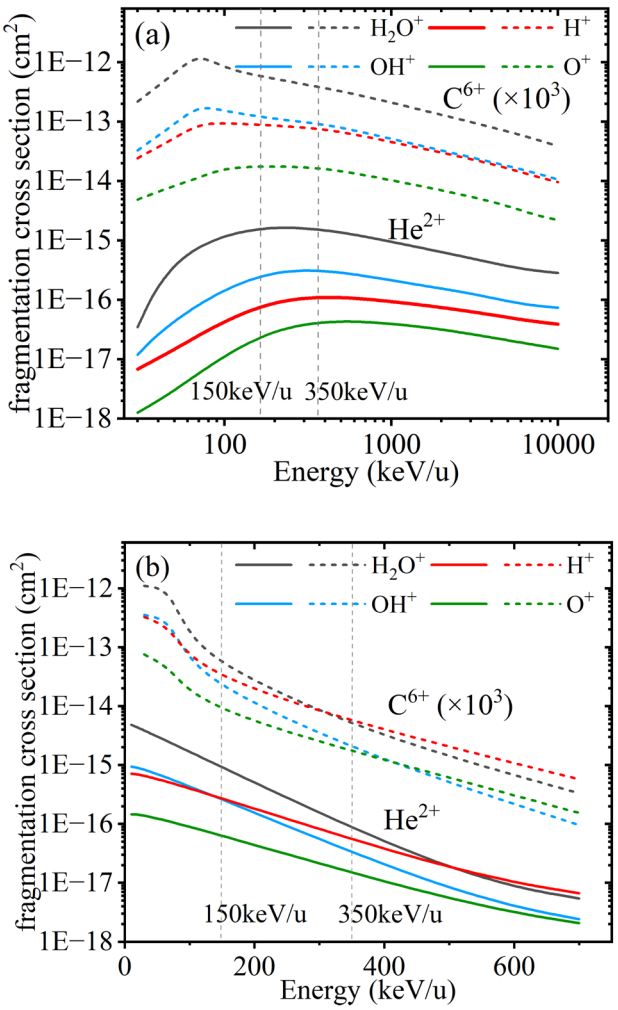

Fig. 11 (Color online) Cross sections for the formation of H_2O^+, OH^+, H^+ and O^+ fragments after **a** SI and **b** SC in He^{2+}+H_2O and C^{6+}+H_2O collisions

fragmentation cross section after SI and SC decreases as the projectile energy increases. Particularly for the fragmentation process after SC, the relative magnitudes of the fragmentation cross sections of H^+ and H_2O^+ as well as of O^+ and OH^+ exhibit discrepancies. (iii) For the fragmentation cross sections after SI, the H_2O^+ fragments are dominant in the energy range around the Bragg peak. For the fragmentation cross sections after the SC, the H_2O^+ fragment dominates in the energy range below the Bragg peak energy, whereas the H^+ fragment dominates in the energy range above the Bragg peak energy.

4 Conclusion

This paper investigates the cross sections of SI and SC and the fragmentation processes for heavy ion (He^{2+} and C^{6+})–H_2O collisions in the energy range around the Bragg peak. The single differential cross section and impact parameter dependence of different molecular orbitals at specific energies were explored. The conclusions are summarized as follows:

(i) The obtained single differential cross section of the electron angle reveals angle distribution discrepancies in the energy range around the Bragg peak. As the projectile energy increases, the emission angle of the electrons gradually transitions from small angles (0° ∼ 30°) to large angles (60° ∼ 120°). For the single differential cross sections of electron energy, the results indicate that the energy distributions of ionized electrons are similar when the projectile energy is equal to, below and above the Bragg peak energy.

(ii) Dependence of SI and SC on impact parameters: When the projectile energy is below the Bragg peak energy, the removal of electrons is associated with large impact parameters. As the projectile energy increases, the removal of electrons can be associated with small impact parameters. For the impact parameter dependence of SC, the dominance of a particular orbital at different energies depends on whether the electrons in that orbital have velocities similar to that of the projectile.

(iii) For the fragmentation cross sections after SI, the H_2O^+ fragments are dominant when the projectile energy is equal to, below and above the Bragg peak energy. For the fragmentation cross sections after SC, the relative magnitudes vary at different energies. In the energy range below the Bragg peak energy, the H_2O^+ fragment dominates. In the energy range above the Bragg peak, the H^+ fragment is dominant.

In summary, a reliable CTMC code was developed to present a microscopic reaction cross-sectional database relevant to heavy-ion radiotherapy. The SI and SC processes and the fragment yields were investigated within the energy range around the Bragg peak. The presented results can help improve our understanding of heavy-ion radiotherapy.

Acknowledgements The authors thank the useful suggestions from Dr. Wentao Hu. The numerical calculations in this paper have been done on the supercomputing system in the Dongjiang Yuan Intelligent Computing Center.

Author Contributions All authors contributed to the study conception and design. Material preparation, data collection and analysis were performed by Guo-Zhuang Li, Cheng-Ye Sun, Rui Cheng, Yan-Shi Zhang, Liang-Wen Chen, Sheng Zhang, Xin-Xia Li and Lei Yang. The first draft of the manuscript was written by Guo-Zhuang Li and Liang-Wen Chen, and all authors commented on previous versions of the manuscript. All authors read and approved the final manuscript.

Data Availability The data that support the findings of this study are openly available in Science Data Bank at https://cstr.cn/31253.11.

sciencedb.j00186.00432 and https://www.doi.org/31253.11.sciencedb.j00186.00432.

Declarations

Conflict of interest The authors declare that they have no conflict of interest.

References

1. H. Liu, C.F. Jin, S.F. Ge et al., Antitumor and radiosensitization effect of $^{12}C^{6+}$ heavy-ion irradiation mediated by radiation-inducible gene therapy. Nucl. Sci. Tech. **27**, 18 (2016). https://doi.org/10.1007/s41365-016-0021-x
2. Z.Q. Wei, Newest progress in cancer therapy with heavy ion beam and considerations. Nucl. Phys. Rev. **14**, 102–104 (1997). https://doi.org/10.11804/NuclPhysRev.14.02.102
3. Z.Q. Wei, B.W. Wei, Application of heavy ion beams in medical treatment. Med. Eng. Phys. **30**, 485–490 (2001) https://api.semanticscholar.org/CorpusID:124122307
4. H.Y. Feng, L.J. Wu, L.X. Yu et al., Mutagenic effect of a keV range N^+ beam on mammalian cells. Nucl. Instrum. Meth. B. **234**, 477–486 (2005). https://doi.org/10.1016/j.nimb.2005.03.005
5. C.L. Guo, J.F. Wang, X.D. Jin et al., Studies on advantages of heavy ions in radiotherapy compared with γ-rays. Nucl. Instrum. Meth. B. **259**, 997–1003 (2007). https://doi.org/10.1016/j.nimb.2007.03.010
6. Y.C. Feng, M. Li, R.S. Mao et al., Transverse emittance measurement for the heavy ion medical machine cyclotron. Nucl. Sci. Tech. **30**, 184 (2019). https://doi.org/10.1007/s41365-019-0699-7
7. Y. Luo, S.C. Huang, H. Zhang et al., Assessment of the induced radioactivity in the treatment room of the heavy-ion medical machine in Wuwei using PHITS. Nucl. Sci. Tech. **34**, 29 (2023). https://doi.org/10.1007/s41365-023-01181-8
8. Q. Li, A. Kitagawa, T. Kanai et al., Therapeutic purpose ^9C beams produced in the secondary beam line at HIMAC. Nucl. Instrum. Meth. B. **222**, 270–284 (2004). https://doi.org/10.1016/j.nimb.2004.01.223
9. W.M. Sun, N. Du, W.D. Tian et al., Secondary and activated X(γ) radiation of SPHIC particle therapy facility. Nucl. Sci. Tech. **32**, 42 (2021). https://doi.org/10.1007/s41365-021-00870-6
10. P.B. He, Q. Li, Impact of different synchrotron flattop operation modes on 4D dosimetric uncertainties for scanned carbon-ion beam delivery. Sec. Radiat. Oncol. **12**, 806742 (2022). https://doi.org/10.3389/fonc.2022.806742
11. Q. Li, L. Sihver, Therapeutic techniques applied in the heavy-ion therapy at IMP. Nucl. Instrum. Methods Phys. Res. **269**, 664–670 (2011). https://doi.org/10.1016/j.nimb.2011.01.125
12. Q. Li, X.G. Liu, Z. Dai et al., Progress in heavy ion cancer therapy at IMP. AIP Conf. Proc. **1533**, 174178 (2013). https://doi.org/10.1002/msp2.22
13. J. Shi, J.C. Yang, J.W. Xia et al., Heavy ion medical machine (HIMM) slow extraction commissioning. Nucl. Instrum. Meth. A. **918**, 76–81 (2019). https://doi.org/10.1016/j.nima.2018.11.014https://www.sciencedirect.com/science/article/pii/S0168900218315602
14. F. Wang, Y. Xiao, J.F. Yan et al., Carbon ion irradiation-induced DNA damage evokes cell cycle arrest and apoptosis via the pRb/E2F1/c-Myc signaling pathway in p53-deficient prostate cancer pc-3 cells. Nucl. Sci. Tech. **32**, 30 (2021). https://doi.org/10.1007/s41365-021-00861-7
15. C.L. Guo, J.F. Wang, X.D. Jin et al., Studies on advantages of heavy ions in radiotherapy compared with γ-rays. Nucl. Instrum. Meth. B. **259**, 997–1003 (2007). https://doi.org/10.1016/j.nimb.2007.03.010
16. Y. Xie, B. Wang, K. Tanaka et al., Enhancement of radiosensitivity of MCF-7 breast cancer cells subjected to X-ray or carbon-ion irradiations. Nucl. Sci. Tech. **259**, 11 (2016). https://doi.org/10.1007/s41365-016-0009-6
17. Z.Z. Wang, W.J. Li, D.J. Zhi et al., Micronuclei induction in human lymphocytes induced by carbon ions exposion along the penetrate depth of ions in water. Nucl. Instrum. Meth. B. **267**, 2521–2524 (2009). https://doi.org/10.1016/j.nimb.2009.06.007
18. X.D. Jin, Q. Li, W.J. Li et al., The hyper-radiosensitivity effect of human hepatoma SMMC-7721 cells exposed to low dose γ -rays and ^{12}C ions. Nucl. Instrum. Meth. B. **245**, 310–313 (2006). https://doi.org/10.1016/j.nimb.2005.11.120
19. Q.F. Wu, Q. Li, X.D. Jin et al., Bystander effect in human hepatoma HepG2 cells caused by medium transfers at different times after high-LET carbon ion irradiation. Nucl. Instrum. Meth. B. **269**, 153–158 (2011). https://doi.org/10.1016/j.nimb.2010.10.012
20. N. Falzone, B. Cornelissen, K. A. Vallis, Auger emitting radiopharmaceuticals for cancer therapy. In: Garcia Gomez-Tejedor, G., Fuss, M. (eds) Radiation Damage in Biomolecular Systems. Biological and Medical Physics, Biomedical Engineering. Springer, Dordrecht. 461–478 (2012). https://doi.org/10.1007/978-94-007-2564-5_28
21. C. Sonntag, Free-radical-induced DNA damage and its repair: A chemical perspective. (2006) https://api.semanticscholar.org/CorpusID:116882690
22. H.F. Ou, B. Zhang, S.J. Zhao, Gate/geant4-based Monte Carlo simulation for calculation of dose distribution of 400 Mev/u carbon ion beam and fragments in water. Nucl. Sci. Tech. **27**, 83 (2016). https://doi.org/10.1007/s41365-016-0097-3
23. P.F. Ma, J.R. Wang, Z.X. Zhang et al., Measurements of absolute electron capture cross sections in He^{2+}-He and Ne^{8+}-O^{2+}, N^{2+}, CH^{4+} collisions. Nucl. Sci. Tech. **34**, 156 (2023). https://doi.org/10.1007/s41365-023-01309-w
24. M.A. Quinto, P.R. Montenegro, J.M. Monti et al., Electron capture by swift ions from molecules of biological interest. J. Phys. B **51**(16), 165201 (2018). https://doi.org/10.1088/1361-6455/aad152
25. D. Schardt, T. Elsässer, D. Schulz-Ertner, Heavy-ion tumor therapy: physical and radiobiological benefits. Rev. Mod. Phys. **82**, 383–425 (2010). https://doi.org/10.1103/RevModPhys.82.383
26. J. Tabet, S. Eden, S. Feil et al., Absolute total and partial cross sections for ionization of nucleobases by proton impact in the Bragg peak velocity range. Phys. Rev. A **82**, 022703 (2010) https://link.aps.org/doi/10.1103/PhysRevA.82.022703
27. T. Märk, F. Egger, Cross-section for single ionization of H_2O and D_2O by electron impact from threshold up to 170 eV. Int. J. Mass Spectrom. **20**(1), 89–99 (1976). https://doi.org/10.1016/0020-7381(76)80035-6
28. A. Bhogale, S. Bhattacharjee, M. Roy Chowdhury et al., Electron emission from water vapor under the impact of 250-keV protons. Phys. Rev. A **105**, 062822 (2022) https://link.aps.org/doi/10.1103/PhysRevA.105.062822
29. U. Werner, K. Beckord, J. Becker et al., 3D imaging of the collision-induced coulomb fragmentation of water molecules. Phys. Rev. Lett. **74**, 1962–1965 (1995) https://link.aps.org/doi/10.1103/PhysRevLett.74.1962
30. H. Luna, W. Wolff, E.C. Montenegro et al., Ionization and electron-capture cross sections for single- and multiple-electron removal from H_2O by Li^{3+} impact. Phys. Rev. A **93**, 052705 (2016) https://link.aps.org/doi/10.1103/PhysRevA.93.052705

31. S. Bhattacharjee, S. Biswas, J.M. Monti et al., Double-differential cross section for ionization of H_2O molecules by 4-MeV/u C^{6+} and Si^{13+} ions. Phys. Rev. A **96**, 052707 (2017) https://link.aps.org/doi/10.1103/PhysRevA.96.052707
32. A. Jorge, M. Horbatsch, C. Illescas et al., Classical-trajectory Monte Carlo calculations of differential electron-emission cross sections in fast heavy-ion collisions with water molecules. Phys. Rev. A **99**, 062701 (2019). https://doi.org/10.1103/physreva.99.062701
33. L. Gulyás, Multicenter continuum distorted wave with eikonal initial state model for single ionization in ion-molecule collisions: differential electron emission from water under energetic ion impact. Phys. Rev. A **11**, 032815 (2023) https://link.aps.org/doi/10.1103/PhysRevA.108.032815
34. D. Ohsawa, Y. Sato, Y. Okada et al., 6.0–10.0-MeV/u He^{2+} -ion-induced electron emission from water vapor. Phys. Rev. A. **72**, 062710 (2005). https://doi.org/10.1103/PhysRevA.72.062710
35. D. Ohsawa, H. Tawara, F. Soga et al., 6.0 MeV/u carbon ion (C^{6+} and C^{4+})-induced secondary electron emission from water vapor. Phys. Scr. **2013**, 014039 (2013). https://doi.org/10.1088/0031-8949/2013/T156/014039
36. S. Bhattacharjee, C. Bagdia, M.R. Chowdhury et al., Energy and angular distribution of electrons ejected from water by the impact of fast $O^{(8+)}$ ion beams. Eur. Phys. J. D **72**(1), 15 (2018). https://doi.org/10.1140/epjd/e2017-80265-8
37. F.S. Zhang, Interactions of heavy ions with biomolecules: a dynamical microscopic approach. Nucl. Phys. Rev. **23**, 23–34 (2006) http://www.npr.ac.cn/en/article/doi/10.11804/NuclPhysRev.23.01.023
38. S. Uehara, H. Nikjoo, Monte carlo track structure code for low-energy alpha-particles in water. J. Phys. Chem. B **106**, 11051–11063 (2002). https://doi.org/10.1021/JP014004H
39. O. Boudrioua, C. Champion, C. DalCappello et al., Ab initio calculation of differential and total cross sections for the ionization of water vapor by protons. Phys. Rev. A **75**, 022720 (2007) https://link.aps.org/doi/10.1103/PhysRevA.75.022720
40. C. Champion, O. Boudrioua, C. DalCappello et al., Theoretical and experimental investigations of electron emission in $He^{2+} + H_2O$ collisions. Phys. Rev. A **75**, 032724 (2007) https://link.aps.org/doi/10.1103/PhysRevA.75.032724
41. T. Liamsuwan, S. Uehara, D. Emfietzoglou et al., A model of carbon ion interactions in water using the classical trajectory monte carlo method. Radiat. Prot. Dosim. **143**, 152–155 (2010). https://doi.org/10.1093/rpd/ncq395
42. M.A. Quinto, J.M. Monti, P.D. Montenegro et al., Single ionization and capture cross sections from biological molecules by bare projectile impact. Eur. Phys. J. D **71**, 35 (2017). https://doi.org/10.1140/epjd/e2017-70652-6
43. T. Liamsuwan, H. Nikjoo, Cross sections for bare and dressed carbon ions in water and neon. Phys. Med. Biol. **58**(3), 641 (2013). https://doi.org/10.1088/0031-9155/58/3/641
44. N. Bachi, S. Otranto, G.S. Otero et al., The role of multiple ionization of H_2O in heavy ion collisions. Phys. Med. Biol. **64**(30), 205020 (2019). https://doi.org/10.1088/1361-6560/ab41db
45. C. Illescas, L.F. Errea, L. Mendez et al., Classical treatment of ion-H_2O collisions with a three-center model potential. Phys. Rev. A **83**, 052704 (2011) https://link.aps.org/doi/10.1103/PhysRevA.83.052704
46. Q. Li, Y. Furusawa, M. Kanazawa et al., Enhanced biological effect induced by a radioactive ^{9}C-ion beam at the depths around its Bragg peak. Nucl. Instrum. Meth. B **245**, 302–305 (2006). https://doi.org/10.1016/j.nimb.2005.11.119
47. Q. Li, Z. Wei, Calculations of heavy ion track structure and energy deposition distribution in liquid water. Nucl. Instrum. Meth. B **122**, 657–662 (1997). https://doi.org/10.1016/S0168-583X(96)00690-8
48. R.H. Garvey, C.H. Jackman, A.E.S. Green, Independent-particle-model potentials for atoms and ions with $36 < Z < 54$ and a modified thomas-fermi atomic energy formula. Phys. Rev. A **12**, 1144–1152 (1975) https://link.aps.org/doi/10.1103/PhysRevA.12.1144
49. C.O. Reinhold, C.A. Falcón, Classical ionization and charge-transfer cross sections for $H^+ + He$ and $H^+ + Li^+$ collisions with consideration of model interactions. Phys. Rev. A **33**, 3859–3866 (1986) https://link.aps.org/doi/10.1103/PhysRevA.33.3859
50. N. Ferreira, L. Sigaud, E.C. Montenegro, Three-body fragmentation from single ionization of water by electron impact: the role of satellite states. J. Phys. Chem. A **121**(17), 3234–3238 (2017). https://doi.org/10.1021/acs.jpca.7b01986
51. K.H. Tan, C.E. Brion, P.E. Van der Leeuw et al., Absolute oscillator strengths (10–60 eV) for the photoabsorption, photoionisation and fragmentation of H_{20}s. Chem. Physics. **29**(3), 299–309 (1978). https://doi.org/10.1016/0301-0104(78)85080-0
52. G.Z. Li, S. Zhang, Z.H. Jiao et al., Charge transfer in collisions of H^+, Li^{3+}, Be^{4+} and O^{8+} ions with He atom based on 4-classical trajectory monte carlo method. Acta. Phys. Sin. **71**, 035201 (2022) https://wulixb.iphy.ac.cn/en/article/doi/10.7498/aps.71.20211470
53. C. Dal Cappello, C. Champion, O. Boudrioua et al., Theoretical and experimental investigations of electron emission in $C^{6+} + H_2O$ collisions. Nucl. Instrum. Meth. B **267**(5), 781–790 (2009). https://doi.org/10.1016/j.nimb.2008.12.010
54. J.P. Biersack, J.F. Ziegler. The stopping and range of ions in solids. In: H. Ryssel, H. Glawischnig (eds) Ion Implantation Techniques. Springer Series in Electrophysics, Springer, Berlin, Heidelberg. **10**, 122–156 (1982). https://doi.org/10.1007/978-3-642-68779-2_5
55. C. Illescas, I. Rabadán, A. Riera, Illustration of the role of saddle-point and molecular-type ionization mechanisms in atomic collisions. Phys. Rev. A **57**, 1809–1820 (1998) https://link.aps.org/doi/10.1103/PhysRevA.57.1809
56. M.E. Rudd, C. Sautter, C.L. Bailey, Energy and angular distributions of electrons ejected from hydrogen and helium by 100–300-keV protons. Phys. Rev. **151**, 20–27 (1966) https://api.semanticscholar.org/CorpusID:120619930
57. Y.Y. Xia, C.Y. Tan, W.N. Lennard, Impact-parameter dependence of the electronic energy loss and angle-dependent energy loss for ions traversing thin foils. Nucl. Instrum. Meth. B **90**, 41–44 (1994). https://doi.org/10.1016/0168-583X(94)95507-7
58. N. Kabachnik, Impact parameter dependence of energy loss and charge exchange in ion-atom collisions. Nucl. Instrum. Meth. B **115**, 292–298 (1996). https://doi.org/10.1016/0168-583X(96)00165-6